Accepted Manuscript

Redox behaviour of a Ceria-Zirconia Inverse Model Catalyst

Michael Allan , David Grinter , Simran Dhaliwal , Chris Muryn , Thomas Forrest , Francesco Maccherozzi , Sarnjeet S. Dhesi , Geoff Thornton

Please cite this article as: Michael Allan , David Grinter , Simran Dhaliwal , Chris Muryn , Thomas Forrest , Francesco Maccherozzi , Sarnjeet S. Dhesi , Geoff Thornton , Redox behaviour of a Ceria-Zirconia Inverse Model Catalyst, *Surface Science* (2018), doi: https://doi.org/10.1016/j.susc.2018.12.005

Highlight:

- Demonstration of the redox behaviour of the mixed ceria zirconia whereby reduction of zirconia is compensated by ceria with the consequence that ceria should be more easily reduced.

Redox behaviour of a Ceria-Zirconia Inverse Model Catalyst

Michael Allan[1], David Grinter[2], Simran Dhaliwal[1,2], Chris Muryn[3], Thomas Forrest[2],

Francesco Maccherozzi[2], Sarnjeet S. Dhesi[2] and Geoff Thornton[1]*

1. Department of Chemistry and London Centre for Nanotechnology, University College London, 20 Gordon Street, London WC1H 0AJ, U.K.
2. Diamond Light Source Ltd, Harwell Science and Innovation Campus, Didcot, Oxfordshire OX11 0DE, U.K.
3. School of Chemistry, University of Manchester, Manchester M13 9PL, U.K.

Corresponding Author: g.thornton@ucl.ac.uk

Abstract

The redox behaviour modification following the addition of zirconia to ceria nanostructures supported on Rh(111) has been investigated using a combination of Low Energy Electron Diffraction (LEED) and X-ray Photoemission Electron Microscopy (XPEEM). Soft X-ray irradiation was employed to reduce $ZrO_{2-x}(111)$ supported on Rh(111) and, by introducing oxygen, the reoxidation process of the thin film was monitored. $CeO_2(111)$ was then deposited on zirconia/Rh(111) and, using XPEEM, we determined that the mixed metal oxide formed a phase-separated structure with $CeO_2(111)$ nanoparticles on top of the zirconia. Upon exposure of $CeO_{2-x}/ZrO_{2-x}/Rh(111)$ to X-ray illumination, the zirconia no longer undergoes any observable reduction while at the same time the ceria is reduced. Our results indicate a synergy between the zirconia and ceria in the phase-separated system expected in the working catalyst, with oxygen transfer between the metal oxides. This sheds light on the mechanism of the enhancement of catalytic properties seen with the addition of zirconia to ceria and highlights the oxygen storage and release ability of ceria.

Introduction

Ceria and ceria-based mixed metal oxides have been widely studied due to their use in applications including heterogeneous catalysis[1], organic synthesis[2], chemical sensing[3] and fuel cells[4]. These applications stem from ceria's readily available and easily interconvertible Ce^{3+} and Ce^{4+} oxidation states as well as its high oxygen storage capacity[1,5]. One important technological area in which ceria is employed is in three-way catalytic converters[6]. These are typically made up of three components, namely a noble metal such as rhodium or platinum, ceria or a ceria-based material and also a support, usually Al_2O_3[7]. The interaction between noble metals and ceria is also of relevance to understand its catalysis of CO oxidation in the water-gas shift (WGS) reaction. This has been studied previously on so-called inverse model catalysts, where ultrathin films of ceria were prepared on the desired noble metal surface [8–13].

The addition of zirconia to ceria leads to the formation of a mixed metal oxide, $Ce_xZr_{1-x}O_2$. This has been shown to enhance the catalytic performance of ceria by increasing the reducibility of the oxide. It results in a greater number of oxygen vacancies, the key component thought to be responsible for the catalytic activity [14]. Addition of zirconia also improves the resistance towards sintering, with the optimal composition for catalytic performance being $Ce_{0.5}Zr_{0.5}O_2$ [15]. The mixed oxide has previously been studied experimentally by STM and XPS in conjunction with computational modelling[16–18]. As for $ZrO_2(111)$, this has been studied extensively using STM, LEED and other surface sensitive techniques including resonant photoemission spectroscopy[19–24].

In this work we focus on the influence of zirconia on the redox behaviour of ceria. We employ micro-focused soft X-rays from a third generation light source to probe and modify the oxidation states of the ceria-zirconia system. The reduction of ultrathin metal oxide films

by an X-ray beam is a methodology that has been extensively studied [11,14,25–30]. We compare the behaviour of the individual metal oxides with that of the mixed metal oxide, making use of previous studies that have investigated the reduction and reoxidation of ceria ultrathin films[26].

Experimental

Synchrotron radiation measurements were carried out using the Elmitec LEEM III spectroscopic photoemission and low-energy electron microscope (SPLEEM) at the Nanoscience soft X-ray beamline (I06) at Diamond Light Source. Here we employed Near-edge X-ray Absorption Fine Structure (NEXAFS) alongside secondary electron XPEEM and µ-X-ray Photoelectron Spectroscopy (µ-XPS).

The Rh(111) single crystal (SPL) was prepared by repeated cycles of Ar+ sputtering and annealing to 1100 K in UHV and 800 K in 1×10^{-6} mbar O_2, followed by a final flash anneal at 1500 K in UHV. This resulted in a well-ordered surface as monitored by LEED, with no contamination seen with XPS, Auger Electron Spectroscopy (AES) (see Supplementary Information) or X-ray Absorption Spectroscopy (XAS). An epitaxial ZrO_{2-x}(111) film was prepared by depositing Zr (99.2%, Goodfellow) onto Rh(111) from an electron-beam evaporator (Focus EFM-3). This was carried out with the sample at 1200 K in 5×10^{-7} mbar O_2 and was followed by further heating for 5 mins and subsequent cooling in oxygen. Epitaxial $Ce_{0.4}Zr_{0.6}O_{2-x}$ was prepared by first depositing Ce (99.9%, Goodfellow) followed by Zr (99.2%, Goodfellow) onto the previously grown ZrO_2(111). This was again carried out with the sample at 1200 K in 5×10^{-7} mbar O_2 and was followed by further heating for 5 mins and subsequent cooling in oxygen. The coverages of the oxides were determined using a calibration of the evaporator using ex-situ atomic force microscopy.

4

The photon energies employed for XPS were as follows: Zr 3d: 250 eV, Ce 4f (on-resonance for 4d-4f excitation): 120.8 eV. Binding energies are referenced to the Fermi level of the Rh (111) substrate. The electron kinetic energy (KE) in the SPLEEM instrument is controlled by applying a potential to bias the sample, namely the start voltage (S.V.). The kinetic energy of the emitted/scattered electrons is given by KE = S.V. - $\Delta\Phi$, where $\Delta\Phi$ is the difference in workfunction between the sample and the instrument and is of the order of a few eV. μ-XPS spectra were acquired by imaging the exit slit of the analyser. This probes a 4 μm^2 area of the sample, corresponding to an energy window of approximately 12 eV and has the advantage of very fast acquisition times (~ 1 second per spectrum).

Results and Discussion

3.1 Redox behaviour of a zirconia thin film

$ZrO_{2-x}(111)$ on Rh(111) was studied initially to examine its photo-reduction and subsequent re-oxidation. Figure 1a shows the LEED pattern obtained from a 6±1 monolayer equivalent (MLE) zirconia film on Rh(111), where one monolayer is defined by a single ZrO_2 trilayer unit. First order Rh(111)-(1 × 1) beams are highlighted in red in the inset. The $ZrO_{2-x}(111)$ lattice is aligned with the substrate, with the (1x1) beams highlighted with black circles in the inset corresponding to a real space unit cell 1.4x larger than the substrate. A 2x2 supercell is also observed, as indicated by the green spots in the inset. These observations, as well as the additional beams from the $ZrO_{2-x}(111)$/Rh(111) interface, are similar to those described by Maurice et. al[22]. Note that in contrast to this earlier work, we use the periodicity notation that has been employed in the more recent and extensive work on $CeO_2(111)$ ultrathin films. Figure 1b is a secondary electron XPEEM image obtained at the Zr M_2 edge. Here a uniform brightness is observed, suggesting an essentially complete and uniform coverage of ZrO_2-

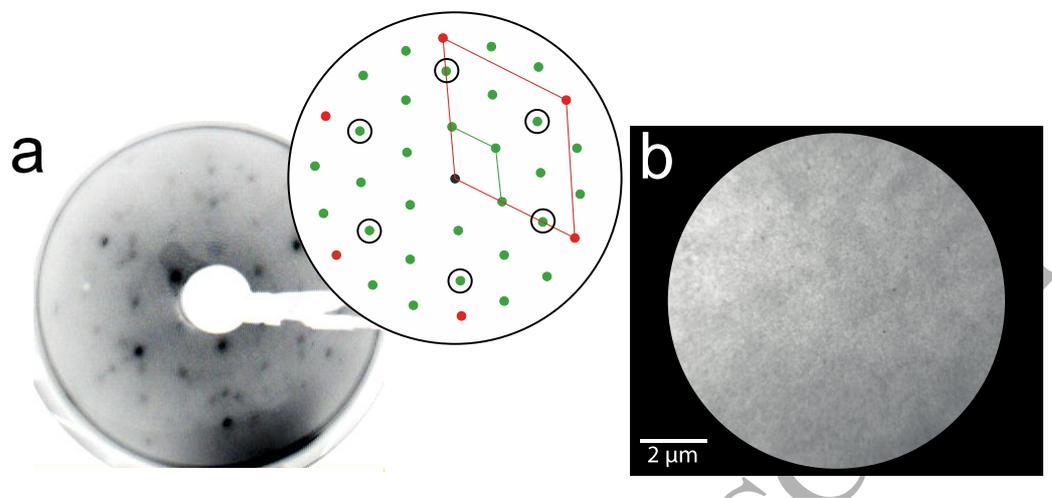$_x$(111) on Rh(111). XAS was used to confirm the presence of Zr as shown in the Supporting Information.

Figure 1: Structure and morphology of a 6±1 MLE ZrO$_{2-x}$(111) ultrathin film on Rh(111). (a) LEED pattern (88.6 eV) of ZrO$_{2-x}$(111)/Rh(111). The beams arising from ZrO$_{2-x}$(111)-(1x1) are highlighted with black circles, p(2x2) are highlighted in green, with substrate spots in red. (b) Secondary electron XPEEM image at the Zr M$_2$ edge (FOV = 10 μm, hν = 349.5 eV).

Figure 2a shows successive plots of the Zr 3d XPS region, which evidence the Zr redox behaviour as it undergoes photo-induced reduction as monitored by μ-XPS. Figure 2b highlights the spectra obtained at various periods of X-ray exposure. In the initial oxidised form (red spectrum), we can see the dominant peak of the Zr^{4+} 3d$_{5/2}$ component (~ 182.7 eV Binding Energy (BE)). As we expose the surface to 250 eV soft X-rays for 140 s (blue spectrum), 350 s (green spectrum) and 500 s (black spectrum), we see a decrease in the Zr 3d$_{5/2}$ peak associated with Zr^{4+}. Concurrently we observe an increase at ~ 180 eV BE, which is indicative of a reduced species, or sub-oxide, being formed. Peak fitting of the sub-oxide region, Figure 2c, shows there are two components, namely sub-oxide A (Zr 3d$_{5/2}$ centered on 180.7 eV BE) and B (Zr 3d$_{5/2}$ centered on 179.2 eV BE). There is some debate over the exact assignment of these species[24,31]. Nevertheless, as they increase upon photo-induced reduction and they appear at a lower binding energy than for the Zr^{4+}, they are assigned here simply to a reduced oxide. The transition from Zr^{4+} to lower oxidation states can be followed through the variation with photon dose of the intensity profile of Zr^{4+} 3d$_{5/2}$ and that for the

6

$3d_{5/2}$ component of the more intense sub-oxide (A) (see Figure 2d). The efficient reduction observed for the zirconia at a photon energy of 250 eV is likely due to the large X-ray absorption cross-section at the $M_{3,4}$ delayed onset[32], assuming a Knotek-Feibelman type mechanism for the photon stimulated desorption of oxygen[33,34].
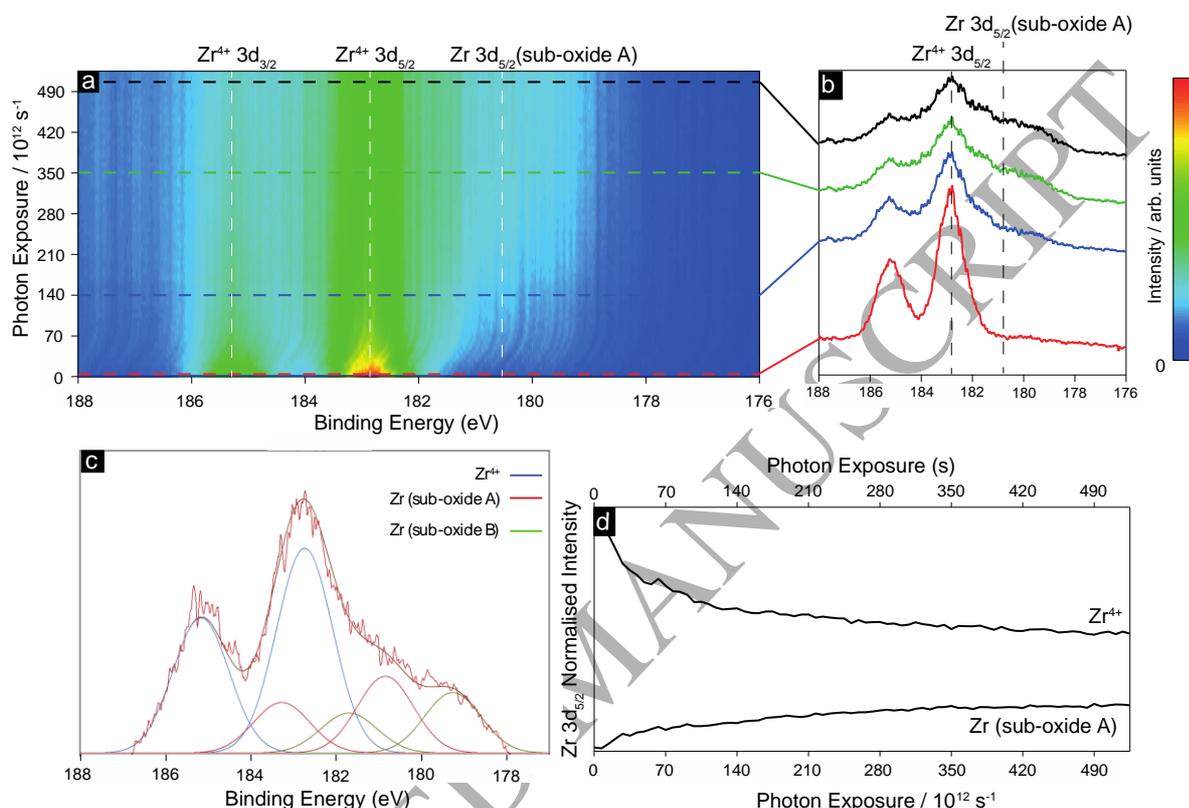

Figure 2: a) µ-XPS Zr 3d spectra (hν = 250 eV, FOV = 2 µm) of 6±1 MLE ZrO_{2-x} on Rh(111) as a function of exposure to the soft X-ray beam. At 0 seconds, the beam was moved to a fresh area which is oxidised and then XPS spectra of 11 eV width centered on the Zr 3d orbitals were obtained over 520 seconds. Data have been corrected for a minor bandbending shift of the Zr 3d peaks, which can be observed in the background. b) Snapshots of the XPS spectra obtained after 0, 140, 350 and 500 seconds of photon exposure. c) µ-XPS of the Zr 3d region recorded after 450 s. Deconvolution of the spectra was performed using Gaussian-Lorentzian lineshapes, after subtraction of a Shirley type background with the full width at half maximum (FWHM) constrained to be equal. d) The evolution with time of the Zr (sub-oxide) and Zr^{4+} $3d_{5/2}$ peaks.

The reoxidation of the reduced film by oxygen was investigated in order to test the reversibility of the x-ray reduction process. The resulting Zr 3d spectra are displayed in Figure 3, showing the effect of ramping the oxygen pressure from 1 x 10^{-8} mbar up to 1 x 10^{-7} mbar. At the start of the experiment, in UHV, the spectrum has major Zr^{4+} components at

182.7 eV BE and 185.1 eV BE but also contains some minor components associated with sub-oxides. At 2 x 10^{-8} mbar, a reversal of the reduction begins with a decrease in the amount of sub-oxide species and an increase in the Zr^{4+} component. By 5 x 10^{-8} mbar, there is a complete reversal of the reduction. Upon removal of the oxygen, immediate reduction is observed to begin again, as shown in Figure 3c.
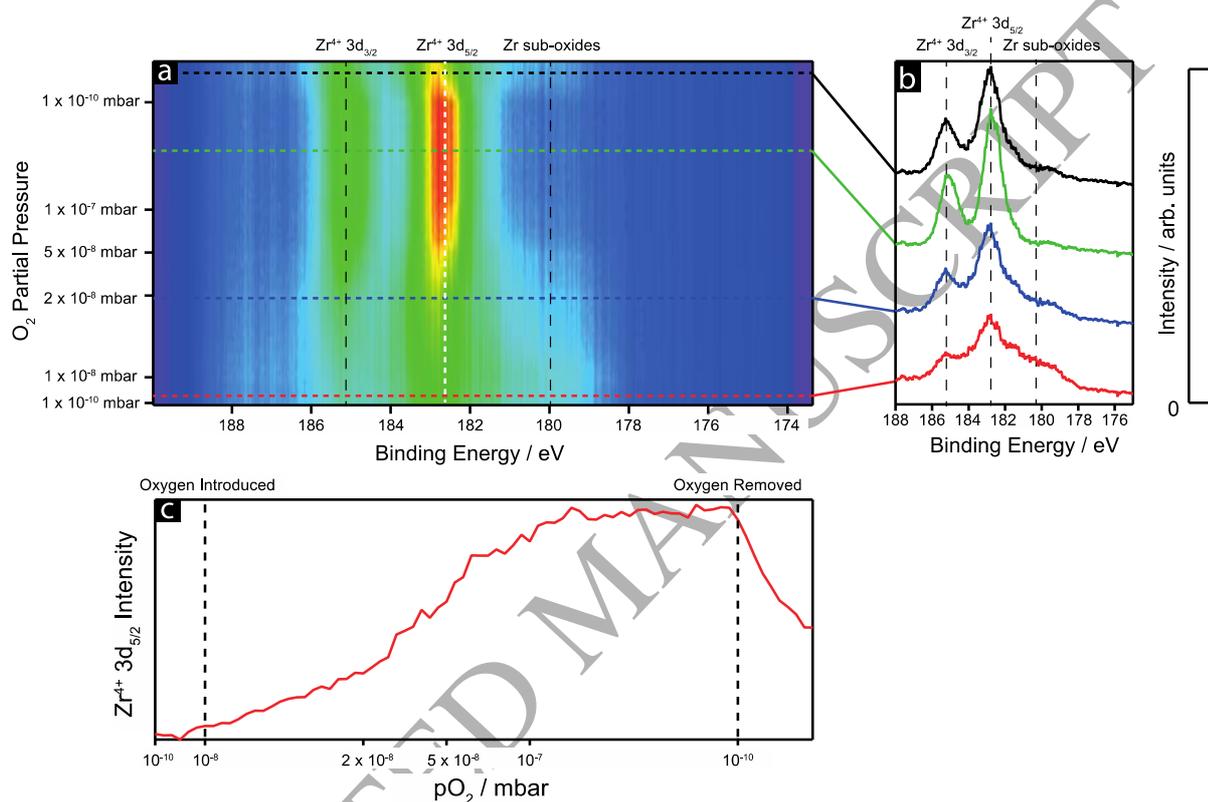

Figure 3: a) μ-XPS Zr 3d spectra (hν = 250 eV, FOV = 2 μm) of 6±1 MLE ZrO_{2-x} on Rh(111) that monitor the reoxidation of a partially reduced zirconia thin film as the pO_2 is increased from 1 x 10^{-8} mbar to 1 x 10^{-7} mbar, showing near complete reoxidation of zirconia at 300 K. b) Selected spectra correspond to the initial reduced thin film (red spectrum), pO_2 at 2 x 10^{-8} mbar (blue spectrum), 1 x 10^{-7} mbar (green spectrum) and once oxygen has been pumped out to 1 x 10^{-10} mbar (black spectrum). c) A line profile showing the change in intensity of the Zr^{4+} $3d_{5/2}$ XPS signal over the range of pO_2.

3.2 Redox behaviour of Zirconia/Ceria Mixed Oxide System

Figure 4 shows the LEED pattern after Ce/Zr reactive deposition onto 6±1 MLE ZrO_{2-x}/Rh(111) followed by annealing to form the model mixed oxide inverse catalyst. Assuming that this additional coverage of oxide remains distinct, the stoichiometry is

$Ce_{0.4}Zr_{0.6}O_{2-x}$. The zirconia spots are still visible, with the (1x1) beams overlapping the CeO_{2-x}(111)1x1 beams at a spacing of (1.4 × 1.4) with respect to the Rh(111)-(1x1) substrate[35]. The interface beams are no longer visible, which is consistent with the formation of a thicker oxide overlayer.
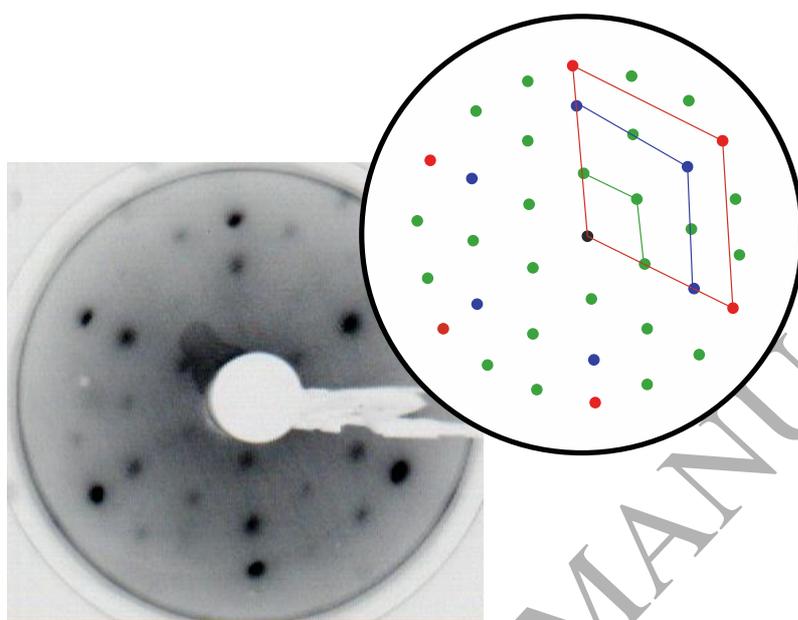

Figure 4: LEED (84.6 eV) pattern of $Ce_{0.4}Zr_{0.6}O_{2-x}$/6±1 MLE ZrO_{2-x}/Rh(111). The spots corresponding to the zirconia are highlighted in green, ceria in blue and the substrate in red. The only apparent difference between this pattern and that in Figure 1 is the addition of intensity to the beams marked in blue, which lie on top of ZrO_{2-x} (111)-(1x1) beams.

In order to examine microscopically the morphology of the mixed metal oxide, secondary electron XPEEM was employed to obtain images at the Ce M_4 and Zr M_2 absorption edges (902 eV and 349.5 eV, respectively). Selected 5 μm snapshots from large-scale (FOV = 10 μm) images are shown in Figure 5a (Ce M_4) and Figure 5b (Zr M_2). In Figure 5a, the ceria nanoparticles are characterised as bright features against a dark background. A number of nanoparticles are highlighted to allow comparisons to other images. In Figure 5b a uniform

brightness is observed with no discernible preference for the highlighted areas of the ceria nanoparticles. What fine structure there is can be ascribed to a spatial variation of detector
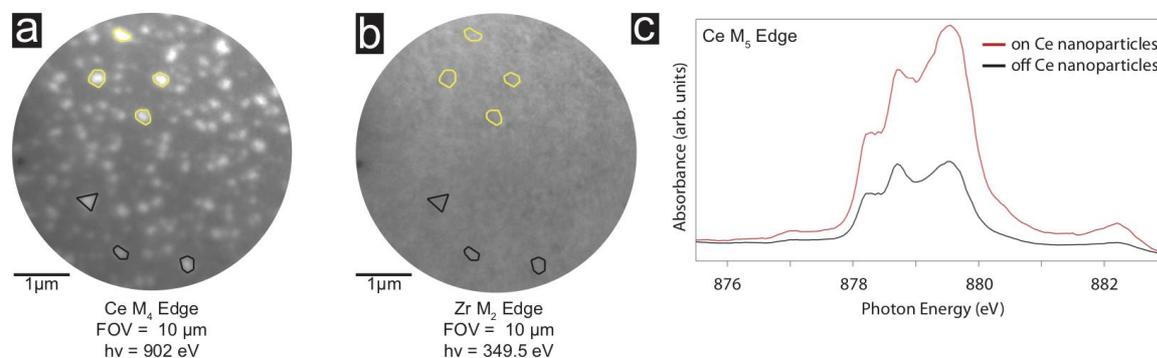

Figure 5: XPEEM identification of $Ce_{0.4}Zr_{0.6}O_{2-x}$ after depositing Ce/Zr on top of $ZrO_2(111)$ whilst annealing in oxygen at 1200 K. 5 µm selected snapshots taken from images recorded with a 10 µm field of view and 2 V start voltage; the images were recorded at the same location at a photon energy of (a) 902 eV and (b) 349.5 eV, which correspond to the Ce M_4 and Zr M_2 edges, respectively. The outlines highlight representative ceria nanoparticles in (a) and their respective location in (b). (c) Ce M_5 edge X-ray absorption spectra on and off the ceria nanoparticles.

efficiency. This suggests that the morphology of zirconia layer covering the substrate is largely unchanged by the decoration with ceria nanoparticles.

Figure 5c shows XAS spectra at the Ce M_5 edge, recorded from a sample of ceria nanoparticles along with areas away from the nanoparticles. Both the M_4 and M_5 edges were probed showing similar intensities and yield similar oxidation state information. Here we can see the preference for cerium within the nanoparticles compared to the background. By comparison of the two, and by reference to model data[26] we see that cerium is more oxidised within the nanoparticles. Comparing XAS spectra taken at the Zr $M_{2,3}$ edge shows no difference between spectra taken on the ceria nanoparticles compared to off the nanoparticles. This is consistent with lack of contrast in the Figure 5b XPEEM image.

10

The XPEEM image in Figure 5a is consistent with a 13% area coverage of the surface. This is also the coverage obtained from ex-situ AFM measurements, where the height of the islands is measured to be about 11 nm. This corresponds to approximately thirty five CeO2 trilayers. This majority phase-separated structure agrees with previous studies and what has been predicted theoretically for active conditions [36]. It was not possible to carry out a complete resonance photoemission spectroscopy experiment to determine the cerium oxidation state of the mixed oxide, but by comparison of the island O 2p/Ce 4f photoemission spectrum to previous work we identify the Ce/O stoichiometry as approximately $CeO_{1.65}$ [25].
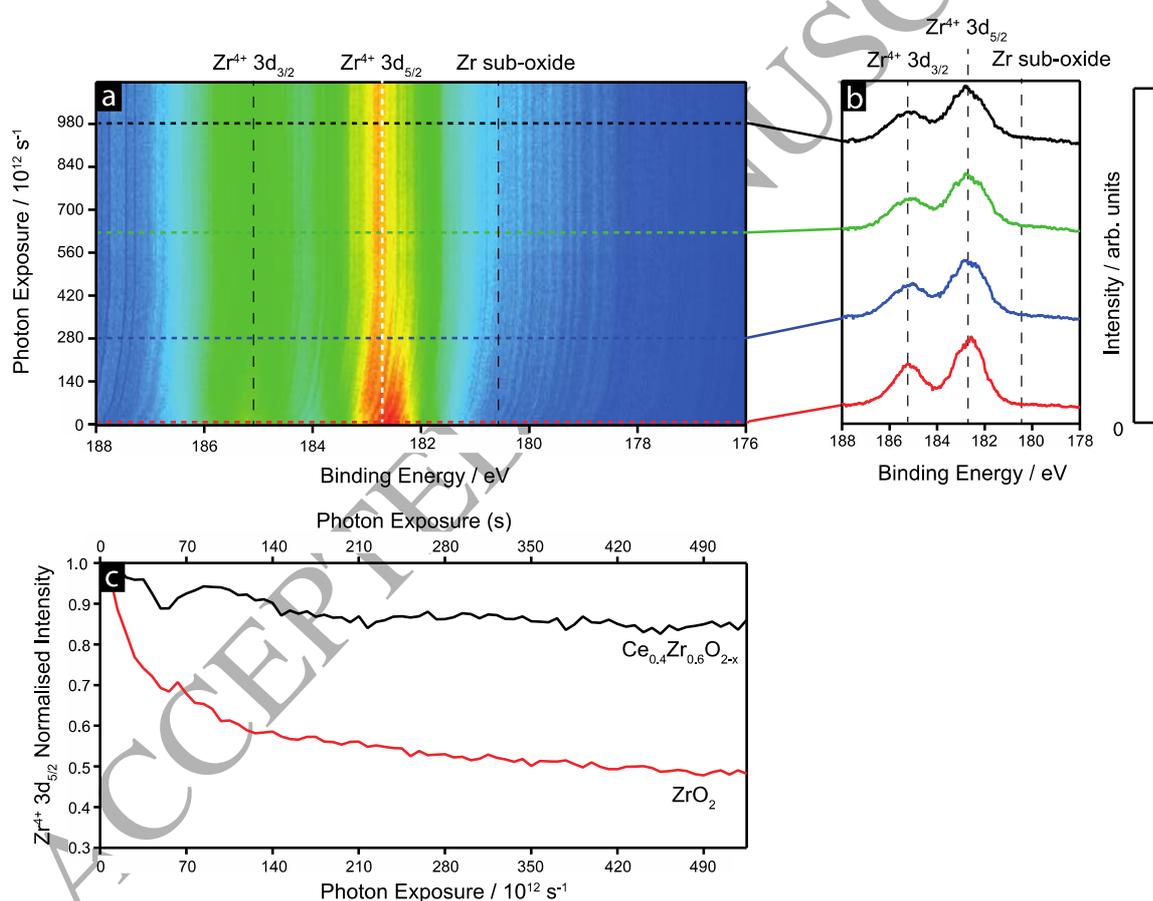

Figure 7: a) μ-XPS Zr 3d spectra (hν = 250 eV, FOV = 2 μm) of $Ce_{0.4}Zr_{0.6}O_{2-x}(111)/6\pm1$ MLE ZrO_{2-x}/Rh(111) as a function of photo-reduction by exposure to the soft X-ray beam. At 0 seconds, the beam was moved to a fresh, unexposed area of the sample which is still fully-oxidised and then XPS spectra were obtained over the next 1000 seconds. Data have been corrected for minor bandbending of the Zr 3d peaks, which can be observed in the background. b) Snapshots of the XPS spectra obtained after 0, 280, 630 and 980 seconds of photon exposure. c) Time evolution of the normalised Zr $3d_{5/2}$ intensity for both ZrO_2 (red) and $Ce_{0.4}Zr_{0.6}O_{2-x}$ (black).

Figure 7 shows successive plots investigating the Zr redox behaviour within $Ce_{0.4}Zr_{0.6}O_{2-x}$ as it undergoes photo-induced reduction, along with a comparison with pure ZrO_{2-x}/Rh(111). Focussing on the spectra obtained at selected lengths of X-ray exposure (Figure 7b), we see much less reduction than observed for zirconia. A comparison of the reduction of Zr within $Ce_{0.4}Zr_{0.6}O_{2-x}$ to what was seen in ZrO_2 is shown in Figure 7c. A steady-state is reached much earlier for the former, after approximately 210 s, with only a 10% reduction in the Zr^{4+} $3d_{5/2}$ in $Ce_{0.4}Zr_{0.6}O_{2-x}$. This compares with 50% for ZrO_2 , which only reaches a steady state after 500 s. This was repeated up to 2000 s to test for further reduction in the mixed oxide, none being observed. By comparing this to ceria reduction as probed by resonant XPS of the Ce 4f contribution to the valence band (see Figure 8) we see that ceria undergoes similar redox behaviour to that seen in previous studies [25,26]. By moving to a freshly oxidised area, Figure 8a shows successive VB spectra at a photon energy of 120.8 eV (on resonance for Ce^{3+}) versus photon exposure with selected spectra shown in Figure 8b. The results in Figure 8c highlight the immediate reduction towards Ce^{3+} upon removal of oxygen and the reoxidation with the introduction of oxygen. This observation that ceria continues to undergo reduction while the reduction of zirconium appears inhibited provides some explanation for the synergy evidenced in reaction studies [37–40], with oxygen transfer occurring between the ceria and zirconia.
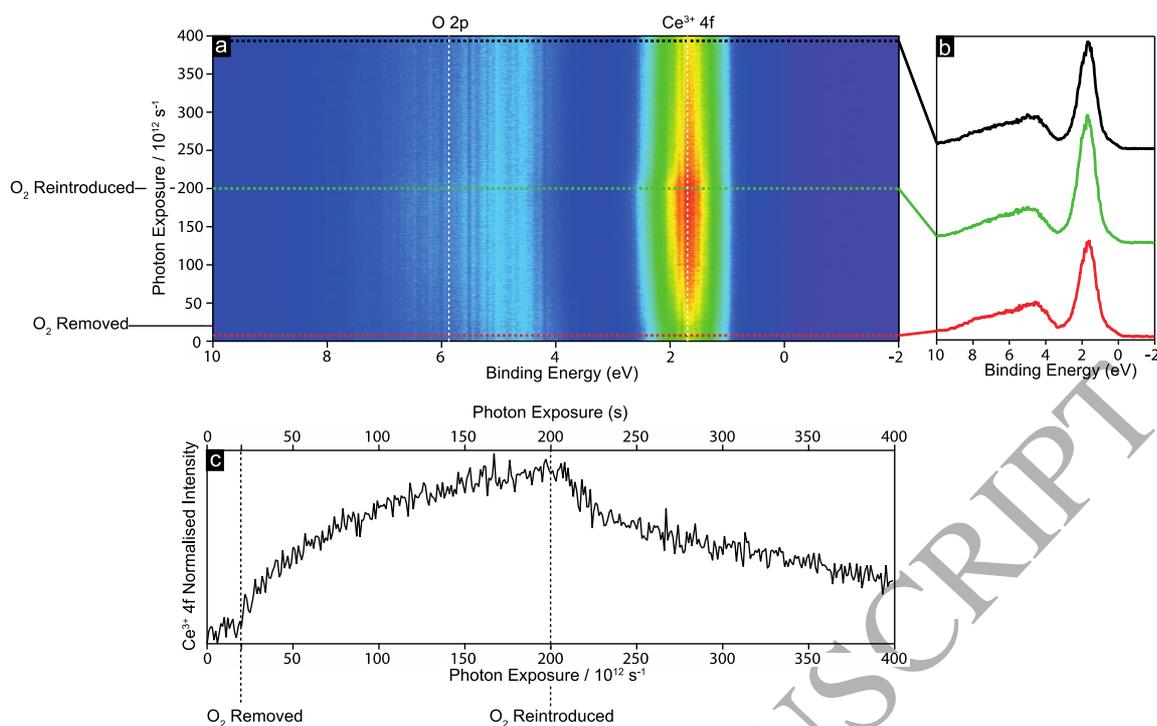
Figure 8: a) μ-XPS valence band spectra of $Ce_{0.4}Zr_{0.6}O_{2-x}(111)/6\pm1$ MLE ZrO_{2-x}/Rh(111) recorded on the Ce^{3+} 4f resonance investigating the effect of illumination with soft X-rays (hν = 120.8 eV, FOV = 2 μm). Upon moving to a freshly oxidised area, oxygen is removed, leading to ceria being reduced, followed by the introduction of oxygen to 1×10^{-7} mbar where ceria begins to reoxidise. b) Selected spectra for the initial oxidised film (red), the reduced film (green) and the reoxidised film (black). c) Time evolution of the Ce^{3+} 4f normalised intensity.

Summary

A model mixed metal oxide of $CeO_{2-x}(111)$ and $ZrO_{2-x}(111)$ supported on Rh(111) has been prepared to probe the redox behaviour of the mixture. Soft X-ray irradiation was used to reduce zirconia with reoxidation occurring upon the introduction of oxygen at 300 K. Upon the addition of ceria, the zirconia no longer undergoes an observable beam-induced reduction, indicating a synergy between the zirconia and ceria with oxygen transfer occurring between the two. Ceria within the mixed oxide was seen to undergo the same redox behaviour as seen in previous studies of ceria ultrathin films. This provides some explanation of the effects of adding zirconia to ceria in order to enhance its catalytic role in such processes as the water gas shift reaction.

Acknowledgements

Graphical Abstract
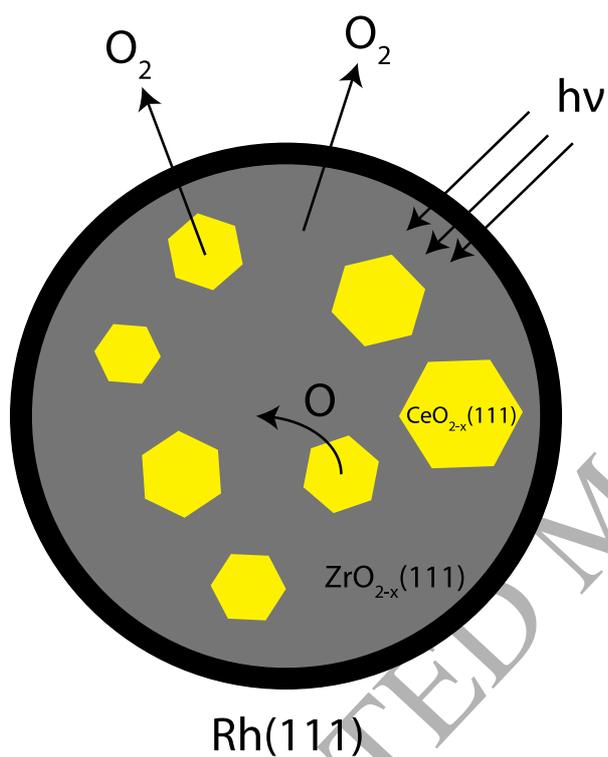
References

[1]   A. Trovarelli, C. de Leitenburg, M. Boaro. G. Dolcetti, Catal. Today 50 (1999) 353–367.

[2]   L. Vivier, D. Duprez, ChemSusChem 3 (2010) 654-678.

[3]   P. Jasinski, T. Suzuki, H.U. Anderson, Sensor. Actuat. B-Chem. 95 (2003) 73-77.

[4]   B.C.H. Steele, Nature 400 (1999) 619-621.

[5]   D.R. Mullins, Surf. Sci. Rep. 70 (2015) 42-85.

[6]   R. Di Monte, J. Kašpar, Top. Catal. 28 (2004) 47-57.

[7]   S. Matsumoto, Catal. Today 90 (2004) 183–190.

[8]   J.A. Rodríguez, J. Hrbek, Surf. Sci. 604 (2010) 241–244.

[9]   T. Ma, S. Surnev, F.P. Netzer, Materials 8 (2015) 5205–5215.

[10]   T. Ducho , F. Dvo ák, M. Aulická, V. Stetsovych, M. Vorokhta, D. Mazur, K. Veltruská, T. Skála, J. Myslive ek, I. Matolínová, V. Matolín, J. Phys. Chem. C 118 (2014) 357–365.

[11]   J. Matharu, G. Cabailh, R. Lindsay, C.L. Pang, D.C. Grinter, T. Skála, G. Thornton, Surf. Sci. 605 (2011) 1062–1066.

[12]   B. Kaemena, S.D. Senanayake, A. Meyer, J.T. Sadowski, J. Falta, J.I. Flege, J. Phys. Chem. C 117 (2013) 221–232.

[13]   C. Rameshan, H. Li, K. Anic, M. Roiaz, V. Pramhaas, R. Rameshan, R. Blume, M. Hävecker, J. Knudsen, A. Knop-Gericke, G. Rupprechter, J. Phys. Condens. Matter 30 (2018) 264007.

[14]   J.A. Rodriguez, X. Wang, P. Liu, W. Wen, J.C. Hanson, J. Hrbek, M. Pérez, J. Evans, Top. Catal. 44 (2007) 73–81.

[15]   R. Di Monte, J. Kašpar, Catal. Today 100 (2005) 27–35.

[16]   S. Hu, W. Wang, Y. Wang, Q. Xu, J. Zhu, J. Phys. Chem. C 119 (2015) 18257–18266.

[17]   A.E. Nelson, K.H. Schulz, Appl. Surf. Sci. 210 (2003) 206–221.

[18]   G. Balducci, J. Kašpar, P. Fornasiero, M. Graziani, M.S. Islam, J. Phys. Chem. B (1998) 557-561.

[19]   K. Meinel, K.-M. Schindler, H. Neddermeyer, Surf. Sci. 532–535 (2003) 420–424.

[20]   K. Meinel, A. Eichler, K.-M. Schindler, H. Neddermeyer, Surf. Sci. 562 (2004) 204–218.

[21]   J.I.J. Choi, W. Mayr-Schmölzer, I. Valenti, P. Luches, F. Mittendorfer, J. Redinger, U. Diebold, M. Schmid, J. Phys. Chem. C 120 (2016) 9920–9932.

[22] V. Maurice, M. Salmeron, G.A. Somorjai, Surf. Sci. 237 (1990) 116–126.

[23] J.M. Sanz, A.R. González-Elipe, A. Fernández, D. Leinen, L. Galán, A. Stampfl, A.M. Bradshaw, Surf. Sci. 307-309 (1994) 848-853.

[24] H. Li, J.I.J. Choi, W. Mayr-Schmölzer, C. Weilach, C. Rameshan, F. Mittendorfer, J. Redinger, M. Schmid, G. Rupprechter, J. Phys. Chem. C 119 (2015) 2462–2470.

[25] D.C. Grinter, C.M. Yim, C.L. Pang, B. Santos, T.O. Mente , A. Locatelli, G. Thornton, J. Phys. Chem. C 117 (2013) 16509–16514.

[26] D.C. Grinter, C. Muryn, A. Sala, C.M. Yim, C.L. Pang, T.O. Mente , A. Locatelli, G. Thornton, J. Phys. Chem. C 120 (2016) 11037–11044.

[27] D.C. Grinter, C. Muryn, B. Santos, B.J. Shaw, T.O. Mente , A. Locatelli, G. Thornton, J. Phys. Chem. C 118 (2014) 19194–19204.

[28] L. Gregoratti, T.O. Mentes, A. Locatelli, M. Kiskinova, J. Electron Spectrosc. Relat. Phenom. 170 (2009) 13–18.

[29] S. Günther, B. Kaulich, L. Gregoratti, M. Kiskinova, Prog. Surf. Sci. 70 (2002) 187-260.

[30] E. Paparazzo, G.M. Ingo, J. Electron Spectrosc. Relat. Phenom. 95 (1998) 301-304.

[31] C. Morant, J.M. Sanz, L. Galán, L. Soriano, F. Rueda, Surf. Sci. 218 (1989) 331-345.

[32] J.J. Yeh, I. Lindau, At. Data Nucl. Data Tables 32 (1985) 1–155.

[33] M.L. Knotek, Reports Prog. Phys. 47 (1984) 1499–1561.

[34] M.L. Knotek, P.J. Feibelman, Phys. Rev. Lett. 40 (1978) 964–967.

[35] D.C. Grinter, C.L. Pang, C.A. Muryn, F. Maccherozzi, S.S. Dhesi, G. Thornton, J. Electron Spectrosc. Relat. Phenom. 195 (2014) 13–17.

[36] R. Grau-Crespo, N.H. De Leeuw, S. Hamad, U.V. Waghmare, Proc. R. Soc. A 467 (2011) 1925–1938.

[37] G. Balducci, M.S. Islam, J. Kašpar, P. Fornasiero, M. Graziani, Chem. Mater. 12 (2000) 677–681.

[38] J.R. González-Velasco, M.A. Gutiérrez-Ortiz, J.-L. Marc, J.A. Botas, M.P. González-Marcos, G. Blanchard, Appl. Catal. B Environ. 22 (1999) 167–178.

[39] P. Fornasiero, G. Balducci, R. Di Monte, J. Kašpar, V. Sergo, G. Gubitosa, A. Ferrero, M. Graziani, J. Catal. 164 (1996) 173–183.

[40] A. Wolfbeisser, O. Sophiphun, J. Bernardi, J. Wittayakun, K. Föttinger, G. Rupprechter, Catal. Today 277 (2016) 234–245.